Research Article | Vol. 1, No. 1 / 15 Jan 2022 / Optics Continuum 16
OPTICS CONTINUUM

Spectral broadening and a prospect for pulse compression of Yb:YAG thin-disk laser pulses by nonlinear SHG in a BBO crystal with time predelay and tilting of the pulse fronts

MARTIN DUDA,[1,2,*] ONDŘEJ NOVÁK,[1] MARTIN CIMRMAN,[1,2] JAROSLAV HUYNH,[1,2] MARTIN SMRŽ,[1] AND TOMÁŠ MOCEK[1]

[1] *HiLASE Centre, Institute of Physics of the Czech Academy of Sciences, Za Radnicí 828, 252 41 Dolní Břežany, Czech Republic*
[2] *Faculty of Nuclear Sciences and Physical Engineering, Czech Technical University in Prague, Břehová 7, 115 19 Praha 1, Czech Republic*
[*] *martin.duda@hilase.cz*

Abstract: Pulse compression by second harmonic generation in a type II nonlinear optical crystal controlled by a time predelay of the faster input pulse is not simple to achieve high-average-power Yb:YAG lasers with wavelength of 1030 nm. The reason is that the borate nonlinear crystals with their excellent thermal properties do not have the optimal ratio of group velocities of the interacting pulses to achieve efficient pulse compression. We have changed the effective group velocities by tilting the pulse fronts at a diffraction grating and imaging the tilted 1.7 ps pulses into the 6 and 8.5 mm thick BBO crystals. As a result, we have measured significant spectral broadening to 4.5 nm, supporting pulses as short as 100 fs, with an energy conversion efficiency in excess of 20 %. The measured data correspond well with numerical simulations. This research opens a way to extend the range of possible applications of Yb:YAG high-average-power thin-disk lasers into the fs regime.

1. Introduction

Sum frequency generation, or more particularly second harmonic generation (SHG) in type II phase-matched nonlinear crystals, with simultaneous compression of the frequency doubled pulses, was established in papers [1,2]. In a type II nonlinear crystal, all three waves interacting in the SHG process experience different index of refraction n and group velocity v_g. If the perpendicularly polarized input pulses do not arrive into the crystal at the same time, but the faster one is predelayed in respect to the slower one, the group velocity mismatch (GVM) can be used to compress the second harmonic (SH) pulse to much shorter duration than is the duration of the input pulses, and the process can be so efficient, that the SH peak power can exceed the peak power of the input fundamental pulse.

The pulse compression, illustrated in Fig. 1, is most effective when the group velocity of the SH pulse is exactly in the middle of the group velocities of the input pulses. Then, when one looks at the generation process from the coordinate system connected to the SH pulse, the two input waves start separately and move in opposite directions with the same velocities toward the SH pulse in the middle. As they approach each other, the SH pulse is generated at their temporal overlap. If the interaction is strong enough, the input pulses are perpetually depleted, their temporal overlap stays small and short SH pulse can be generated very efficiently.

The strength of the interaction and the difference between the group velocities impose a limit onto the crystal thickness and the particular time predelay.

Finding a suitable nonlinear crystal, where the condition on group velocities for the selected wavelength is satisfied, is not an easy task. There have been reports on using KDP or DKDP

#437879 https://doi.org/10.1364/OPTCON.437879
Journal © 2022 Received 14 Jul 2021; revised 10 Dec 2021; accepted 13 Dec 2021; published 13 Jan 2022

OPTICS CONTINUUM

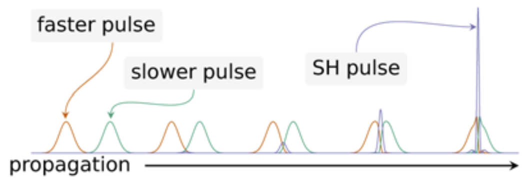

Fig. 1. Sketch of pulse compression mechanism showing the evolution of the SH pulse in different propagation positions.

crystal for SHG of Neodymium doped lasers with a wavelength around 1.05 µm [3–5]. Particularly, [3] used Nd:YLF laser at wavelength of 1054 nm and measured fivefold compression of 1.2 ps pulses, [4] compressed 11 ps long pulses from Nd:YAG laser at wavelength of 1.06 µm up to 32 times. The 1.5 ps long pulses with wavelength of 1053 nm coming from Nd:YAG oscillator and amplified in Nd:glass active medium were frequency doubled and compressed to 0.6 ps in paper [5].

Different set of wavelengths and crystals have been used in [6]. The authors used approximately 1 ps long pulses, the first input wave had wavelength of 1055 nm and the second one between 1400 to 2200 nm. They generated compressed pulses at $600 - 720$nm in BBO crystal, and they compressed the pulses down to 160 fs. In [7], 160 fs long pulses from travelling wave parametric amplifier pumped by Ti:Sapphire laser were also compressed in BBO crystal down to 34 fs. The wavelengths of the input pulses were 1.3 µm and 1.95 µm, with the resulting wavelength being around 780 nm.

The BBO crystal has much lower linear absorption than both the KDP or DKDP crystals at the near infrared wavelength, where high-average-power Yb:YAG thin-disk lasers with pulse durations around 1 ps, as those developed in our centre [8–10], emit their radiation. So even though the group velocities in the (D)KDP crystals are much more suitable for pulse compression, thermal de-phasing limits their use, and BBO crystal is preferred. The group velocities in the BBO crystal are far from ideal, the group velocity of the SH pulse is lower than the group velocities of both input pulses. Some SHG pulse compression of Yb:YAG lasers in BBO crystal with time predelay was first reported in [11] with very few experimental details, and later in [12,13], but the compression mechanism was mainly back-conversion.

To change the effective group velocities of the extraordinarily polarized pulses, one can tilt their pulse fronts by e.g. diffraction grating, as has been proposed in papers [14,15]. Particularly, [14] compressed 1.3 ps long pulses from Nd:glass laser in 3.8 mm thick BBO crystal down to 0.3 ps. Paper [15] used this technique for third harmonic generation.

How the tilting of the pulse fronts changes the effective group velocities is shown for the case of temporal walk-off compensation in a negative uniaxial crystal such as BBO or (D)KDP, and two perpendicularly polarized pulses in Fig. 2. The compensation, however, is not the goal, because certain temporal walk-off is the main ingredient of the pulse compression scheme, and serves only as an illustration. The change in group velocities Δv_g can be calculated by

$$\Delta v_g = v_g \tan \rho \tan \alpha, \tag{1}$$

where ρ is the spatial walk-off angle and α is the internal pulse tilt angle.

In paper [16] we have shown by extensive numerical simulations, that it should be possible to use the BBO crystal for efficient pulse compression, when the pulse-front tilt angle is around 23.5°. Then, the SH group velocity is equal to the mean of the group velocities of the input pulses, and with the Fourier transform limited IR pulses with a duration of 1.7 ps, one can achieve almost 20-fold compression to around 90 fs, with a conversion efficiency almost 50 %, when the thickness of the crystal is around 8.5 mm, the predelay is around 2.2 ps and the peak intensity is between 15 and 20 GW /cm^2.

OPTICS CONTINUUM

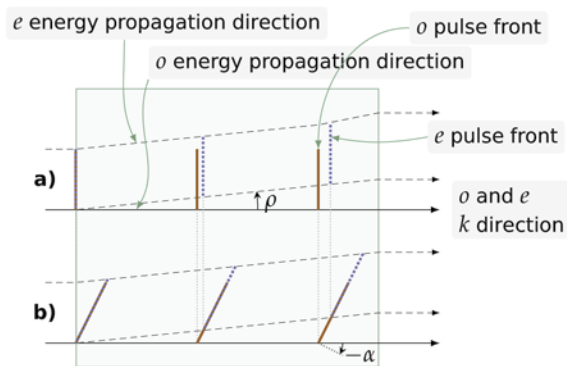

Fig. 2. Geometrical illustration of a temporal walk-off compensation by tilting of the pulse fronts by an angle α in respect to the phase fronts, which remain perpendicular to the crystal input face. Three distinct positions in the crystal are shown. Dotted purple line is extraordinary polarized faster pulse with spatial walk-off angle ρ, orange solid line is ordinarily polarized slower pulse. Without pulse tilting (a), the pulses separate as they propagate through the crystal (green box). With tilting (b), spatial walk-off contributes to the group velocity and compensates for the temporal walk-off – there is no separation in time and the pulses stay overlapped, when propagating.

In this paper, we follow the numerical simulations and present the first experimental evidence of spectral broadening by SHG in type II phase-matched BBO crystal, where the effective group velocities are adjusted by tilting of the pulse fronts while the rate of compression is controlled by predelay. The actual pulse compression was not observed. We carefully describe the experimental details, identify problems with the current measurement and propose solutions, which should allow for efficient pulse compression in the future. We believe, that after the proposed improvements are made, this nonlinear pulse compression technique could extend the range of possible applications of Yb:YAG lasers into the fs regime.

2. Experimental methods

2.1. Experimental setup

The experimental setup is shown in Fig. 3 and consists of three parts, responsible for predelay (green in the figure), pulse-front tilt+SHG (blue) and diagnostics (red).

The predelay is realized by a half-wave plate and a polarizing beam splitter, which divides the fundamental pulse into two orthogonally polarized pulses. The horizontally polarized pulse is directed onto two mirrors mounted on two perpendicular translation stages. The motorized translation stage moving in the beam direction is responsible for the predelay and the other translation stage allows one to easily pre-compensate the spatial walk-off in the critical plane, perpendicular to the orientation of the grooves in the diffraction grating. If the two mirrors are perpendicular to each other, then the movement of this second stage will shift the beam position, but not the direction of propagation or the predelay. The horizontal plane in laboratory is equivalent to the plane containing extraordinary polarization in the nonlinear crystal. Extraordinary polarization is the faster one in the BBO crystal and has to be predelayed. Increases in the translation stage position by ≈ 150 μm causes a predelay of 1 ps, since the laser pulse travels the distance two times. After predelay, both pulses are recombined in another polarizing beam splitter.

Next, there is a diffraction grating causing the angular dispersion. The internal pulse-front tilt angle of 23.5° translates to an external angle of 34.6° for the ordinarily polarized pulse and

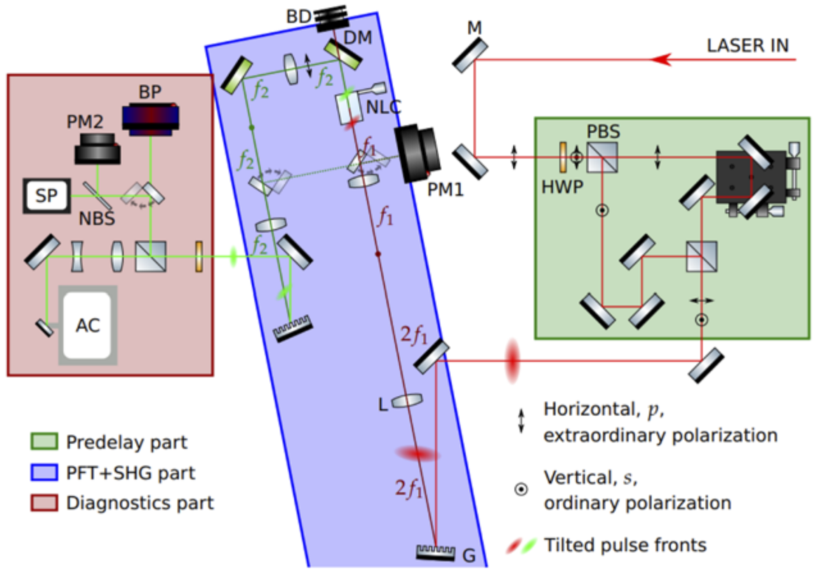

Fig. 3. Experimental scheme used for pulse shaping experiments with tilted pulse fronts. Shown are also the polarization of the laser beam in different parts along the optical path and the tilted pulse fronts. Legend: M – mirror, HWP – half-wave plate, PBS – polarizing beam splitter, G – diffraction grating, L – lens, PM – power meter, NLC – nonlinear crystal, DM – dichroic mirror transmitting first harmonic and reflecting second harmonic, BD – beamdump, AC – autocorrelator, NBS – non polarizing beam splitter, SP – spectrometer and BP – beam profiler.

36.1° for the extraordinarily polarized pulse . Note, that we use the effective group velocities for the calculation. For the SH pulse, the outside pulse-front tilt angle will be 35.4°. Since it is not practical to tilt each of the input pulses separately, they were tilted approximately to the same value with one diffraction grating. Due to the limited damage threshold of the stock diffraction gratings, we needed lower peak intensity at the first diffraction grating than at the nonlinear crystal. We used a diffraction grating with 300 lines /mm and a telescope with lenses of focal lengths $f1 = 250$ mm and $f_1/2 = 125$ mm and angular magnification of 2 to image the grating onto the nonlinear crystal. The grating was blazed for the wavelength of 1 µm, the blaze angle was 8°36′. We used incidence angle of 3.3°, resulting in pulse-front tilt angle of 32.6°. The SH beam was imaged by a non-magnifying telescope onto a second diffraction grating with 1200 lines /mm and blaze angle of 17°27′ under the incidence angle of 12.5° to cancel the angular dispersion and the pulse front tilt by 34°. It is important to note, that the gratings have different diffraction efficiencies for each polarization. We changed the ratio between the energies in both input polarizations by the half-wave plate in the predelay part of the setup and we measured the energies in both beams after the first diffraction grating, to obtain the ration of energies inside the crystal 1 : 1. The need for the imaging optics and its influence on the pulse-front tilting is discussed in papers [17,18].

We used two BBO crystals for the experiments. Both had dual wavelength AR coating at both faces, aperture of 8×8 mm^2, one had a thickness of 6.12 mm and the second one was 8.45 mm thick. They were cut for type II phase matching with $\theta = 33.7°$ and $\varphi = 0°$ ($eo \rightarrow e$ interaction), and were operated at a room temperature.

The input laser power was measured after the first diffraction grating, before the nonlinear crystal, and the SH power was calibrated to a power measured after the second dichroic mirror and before the second grating. Thus, we can neglect the diffraction efficiency in our analysis.

OPTICS CONTINUUM

Ophir 50(150)A-BB-26 thermopile power meter was used for the calibration of the SH power and measurement of the input power (PM1 in the experimental scheme), and Ophir 3A thermopile power meter for the continuous SH power monitoring (PM2). The SH spectrum was measured with Narran spectrometer BR8 in second diffraction order. For the beam profile measurement, motorized flip mounts were added to switch between the diagnostics branches. Beam profiles were measured with Cinogy CinCam CMOS 1.001 nano. The autocorrelation was measured with APE pulseCheck device. Since the beam was larger than was the size of the input aperture of the autocorrelator, the beam size was reduced four times by a telescope. Mention of vendor names and model numbers is for technical communication purposes only and does not necessarily imply recommendation of these units, nor does it imply that comparable units from another vendor would be any less suitable for this application.

The driving laser pulse had a duration of 1.7 ps according to the autocorrelation measurement and a Gaussian fit, see Fig. 4(a), and was slightly chirped in frequency, with the value of the chirp being around 0.2 THz /ps. This value was measured by frequency-resolved optical gating (FROG). We fitted the temporal phase by a fourth-order polynomial and used the fitted parameter for the quadratic term as the chirp value. The M^2 parameter was approximately 1.1, the beam diameter was 4.76 mm, slightly elliptical with ellipticity of 0.89, see Fig. 4(b). The total energies used for experiments were 2.35 and 3.10 mJ, resulting in a peak intensities of 15.0 and 19.8 GW /cm^2, respectively. The repetition rate of the laser was 1 kHz in order to have low power and safer environment for experiments, but there is no problem with eventual use of higher repetition rates and higher average powers.

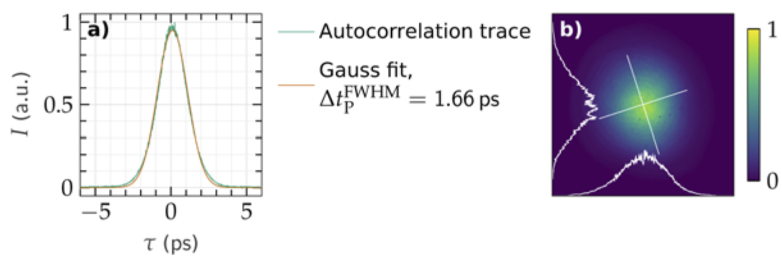

Fig. 4. Autocorrelation measurement and Gaussian fit (a) and a beam profile (b) of the driving laser.

2.2. Measurement procedure

First, the position of zero predelay and the proper orientation of the nonlinear crystal was determined with the use of the following behaviour. At pulse-front tilt angle of 23.5°, there is a large difference between the group velocities of the input pulses and the v_g of SH pulse is just in the middle of them. At $\alpha = -23.5°$, there is very small difference between the group velocities of the input pulses and the v_g of the SH pulse is significantly slower, see Fig. 5ab.

From the group velocities, when there is a weak energy exchange, one should expect a plateau of the conversion efficiency for the positive pulse-front tilt angle, because for some predelay range, the input pulses meet somewhere in the crystal and generate the SH beam in similar way. However, when the pulse-front tilt angle is negative, efficient SH generation will only happen, when the input pulses are already synchronized at the input face of the crystal. They will generate the SH pulse for a longer time, so more efficiently, than is the case for the positive pulse-front tilt angle. However, as the predelay changes from zero position, the efficiency will drop quickly. Also, the case for negative predelay should be symmetrical in respect to its maximum, contrary to the case with positive pulse-front tilt angle.

OPTICS CONTINUUM

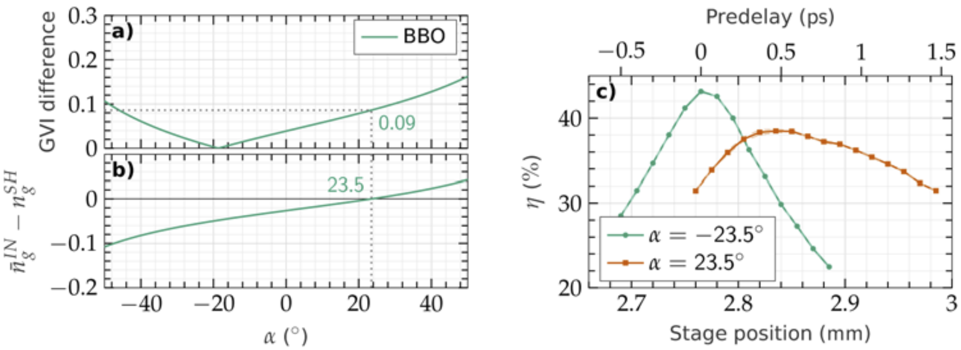

Fig. 5. Difference between group indexes of refraction – group velocity index (GVI) difference – of the input pulses (a) and difference of the group index of refraction of the SH pulse and the mean of the group indexes of the input pulses (b) in dependence on the pulse-front tilt angle α. The energy conversion efficiency η curves across a varying predelay of the faster pulse, measured with two orientations of the nonlinear crystal (c) and thus two signs of the same pulse-front tilt angle α. Calibration between the position of the translation stage and predelay in units of ps is shown with the top axis. The data were measured with the shorter, 6 mm thick crystal, with fundamental power around 0.6 mJ and phase-matched for maximum efficiency at stage position of 2.8 mm.

This was confirmed by a measurement, sample measurement with the shorter crystal is shown in Fig. 5(c). Zero predelay was calibrated to the maximum of conversion efficiency with negative α, and was at the same position of the translation stage for both crystals. Positive predelay refers to the faster pulse trailing the slower one.

All of the devices for diagnostics were calibrated and background was subtracted. The SH beam was aligned into the autocorrelator for maximum efficiency at low energy (around 0.3 mJ of input energy at the nonlinear crystal), where the SH beam profile was still circular, symmetrical and smooth.

We did not particularly focus on the tilting of the nonlinear crystals to achieve phase matching. We used low energy of 0.3 mJ and tilted the crystal to get the highest conversion efficiency. However, to limit the significance of the frequency chirp of the driving laser, it would be appropriate to readjust the phase mismatch for the shortest SH pulse at the correct predelay and energy, same as the spatial walk-off pre-compensation, and find the best operating conditions iteratively.

Next, the SH beam and pulses were characterized for 40 different predelays ranging from −0.4 to 3.5 ps, with a step of 0.1 ps. Both crystals were used for the measurement at the two already mentioned energies.

Based on the numerical simulations from paper [16], output pulses are expected to be shaped and not have Gaussian or sech^2 temporal profile. Normal fitting procedure for these pulse shapes does not work. We decided to fit the autocorrelation traces with a sum of two functions representing the autocorrelation (subscript AC) trace of the sech^2, normally defined by the following equation:

$$I_{\mathrm{AC}}(\tau) = b\frac{3}{\sin^2}\left(\frac{2.7196\times(\tau+c)}{\Delta\tau_{\mathrm{AC}}^{\mathrm{FWHM}}}\right)\times\left[\frac{2.7196\times(\tau+c)}{\Delta\tau_{\mathrm{AC}}^{\mathrm{FWHM}}}\times\coth\left(\frac{2.7196\times(\tau+c)}{\Delta\tau_{\mathrm{AC}^{\mathrm{FWHM}}}}\right)-1\right], \quad (2)$$

where τ is the delay, and the fitting parameters are the amplitude b, the position of the centre c, and the full width half maximum (FWHM) width of the autocorrelation trace $\Delta\tau_{\mathrm{AC}}^{\mathrm{FWHM}}$. We used sum of two such functions, $I_{\mathrm{AC},1}(\tau) + I_{\mathrm{AC},2}(\tau)$ with total of six parameters of the fit for the fitting procedure. In Fig. 6 one can see, that this fitting function achieves a very good cover with the simulated shape of the autocorrelation trace. The duration of the pulse $\Delta t_\mathrm{P}^\mathrm{fit}$ is calculated from the width of the shorter fitting function divided by 1.54 and from the parameters in the legend of Fig. 6, one can see that this pulse duration is still by about 17 % longer than the actual pulse duration.

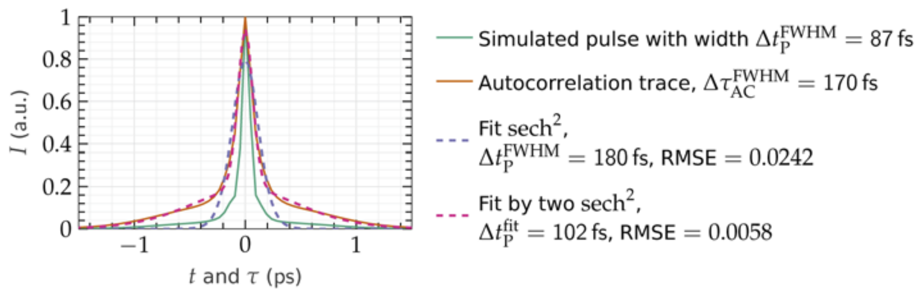

Fig. 6. Temporal profile of the numerically simulated pulse with the highest output power, together with its autocorrelation trace and fitting by one and sum of two fitting functions representing sech^2 pulse shape. In the legend, $\Delta t_\mathrm{P}^\mathrm{FWHM}$ refers to the FWHM pulse duration and $\Delta\tau_\mathrm{AC}^\mathrm{FWHM}$ refers to the width of the autocorrelation trace, with RMSE being the root mean squared error.

3. Results

Throughout multiple graphs, we will present results for the lowest and the highest measured energy and both crystals, always in dependence on predelay of the faster pulse.

3.1. Conversion efficiency

The conversion efficiencies are shown in Fig. 7. The simulated curves were calculated with a phase mismatch of $\Delta k = 0.05$ mm^{-1}, which was estimated as reasonable by comparing simulations and experiments of type I SHG published in [19]. The chirp of the driving pulses was omitted in the majority of calculations. If it was included, it will be noted specifically at an appropriate place. The simulated curves of conversion efficiencies are divided by a factor of two to better compare their shape with the experiment.

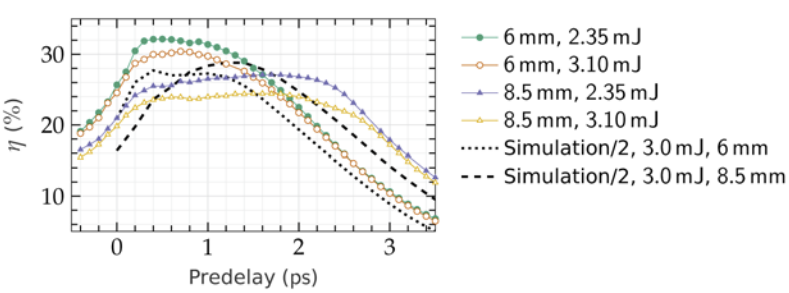

Fig. 7. Measured and calculated energy conversion efficiency η in dependence on predelay. Note on the legend: The circles refer to the shorter crystal and triangles to the longer one. Solid symbols are reserved for the lower energy and the hollow ones for the higher energy. This holds true in all the presented graphs, where applicable.

For the 6 mm thick crystal, the shape of the efficiency curve matches very nicely the simulated one. There is a plateau between 0.3 ps and 1.2 ps. On the negative predelay side, the efficiency

OPTICS CONTINUUM

decreases more sharply than on the positive predelay part, which is exactly what one would expect. The absolute magnitude of the efficiency is slightly more than half of that of the simulated one.

For the thicker crystal, the measured plateau is about three times longer than the simulated one, and the efficiency is even lower than for the thinner crystal. One can, however, observe, that at the right side of the graph, the efficiency is higher in the longer crystal, and it is the other way around on the left side of the graph. This corresponds with the simulations. One can notice one more thing – the efficiency is higher at lower energies.

We presume, that there is a phase mismatch caused by periodic modulation in the beam profile, which will be discussed later in section 3.3, and which was unaccounted for in the simulations. The increased phase mismatch results in much higher rate of the back-conversion, with bigger energy and thicker crystal even more pronounced, and which does not allow for the resulting SH power to be so high. Due to this fact, one cannot see the high peak in the 8 mm crystal and instead, there is only the wide plateau. Outside of this region, the efficiency behaves according to the expectations, but is approximately two times smaller, which can be again caused by the beam aberrations.

3.2. Spectrum

Spectral profiles and their parameters are shown in Fig. 8.

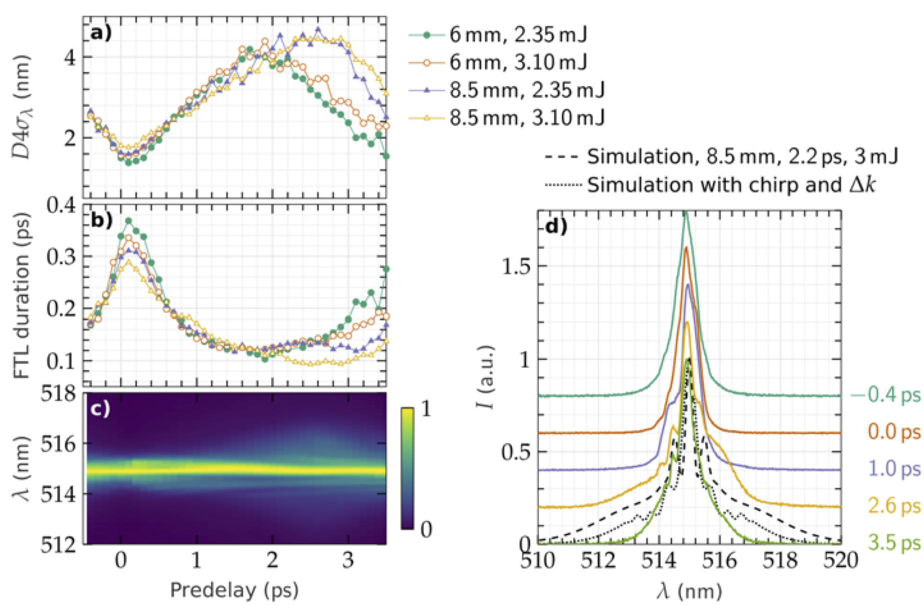

Fig. 8. Spectral width $D4\sigma_\lambda$ (a) and duration of the Fourier-transform limited pulse (b) in dependence on predelay. All spectral profiles measured in 8.5 mm long crystal at an energy of 3.10 mJ in dependence on predelay (c) and measured spectral profiles at chosen predelays compared with numerical simulation (d). Two simulated curves are shown – dashed one with phase mismatch of $\Delta k = 0.05\ \mathrm{mm}^{-1}$ used in the most of the simulations, and dotted one with a chirp of 0.3 THz /ps and $\Delta k = 0.2\ \mathrm{mm}^{-1}$.

Around zero predelay, the spectrum is the narrowest and the Fourier-transform limited duration, calculated by a fast Fourier transform algorithm with the assumption of a flat spectral phase, is the highest. For the 6 mm crystal, the maximum of the spectral width is around 1.9 ps predelay and then it decreases. For the 8.5 mm crystal, the maximum is around 2.5 ps. The minima of the Fourier-transform limited duration correspond to the respective maxima of the spectral width. At higher energy, the spectrum is consistently wider and Fourier-transform limited duration shorter, with the absolute minimum being below 100 fs.

From the spectra one can also tell, that the back-conversion is not the main culprit behind spectral broadening, because the maximal back-conversion is at smaller predelays, where the pulses have enough time to interact. On the other hand, the maxima of the spectral width are at larger predelays, where the pulses meet just at the end of the crystal and do not have so much time to interact between each other. So the spectral broadening truly occurs due to the meeting of the pulses and generation of the short SH pulse, as was intended and expected, based on illustration in Fig. 1.

How do the spectral profiles look like is visible in Fig. 8(c). The image was measured with the 8.5 mm thick crystal at the 3.10 mJ input pulse energy. The originally more or less Gaussian spectral profile gets narrower peak and wide low intensity wings with increasing predelay, with the widest wings being around predelay of 2.6 ps. There are also small side peaks visible at the lower wavelength side of the spectrum, which was also simulated.

Direct comparison of particular spectral profiles with a calculated spectral profile is in Fig. 8(d). The width of the spectral profile is the lowest at zero predelay and as the predelay increases, new side peak starts to appear at the lower wavelength part of the spectrum. At the optimal predelay of 2.6 ps the spectrum is the widest, with the pedestal ranging from below 512 nm to more than 518 nm. In the redder part of the spectrum, the side peaks are less pronounced. The positions of the side peaks coincide well with the side peaks in the simulated spectrum, but are less intense in respect to the central peak, and there is more of them. This is probably caused by the interplay between the frequency chirp of the driving pulses and the increased phase mismatch, as is revealed from the numerical simulations. The spectrum is asymmetric, but this stems from the asymmetry of the spectrum of the driving laser beam. The 2nd moment spectral width of the broadest spectrum is 4.45 nm, almost two times lower than is the width of the simulated spectrum, which is 8.1 nm. The width of the spectrum simulated with chirp of 0.3 THz /ps and with a phase mismatch of $\Delta k = 0.2\ \mathrm{mm}^{-1}$ is 5.5 nm, and that is already a value close to the measured one. The chirp 0.3 THz /ps used in the simulation was chosen as the maximum value of the chirp of the driving laser, with the exact value being usually around 0.2 THz /ps, but dependent on the different fitting results across multiple FROG traces. The phase mismatch was chosen to minimize the simulated pulse duration. For smaller temporal chirp, lower phase mismatch would be enough to compensate it. To add one more perspective to the spectral width: the $D4\sigma_\lambda$ of the SH spectral profile, when the SH beam is generated in type I LBO crystal with the same driving laser [19] and without any pulse compression, is 1.04 nm. Thus, the spectral width measured in current experiments is by 20 % lower than the calculated one, but still more than four times larger than the one obtained without implementing any pulse shaping technique. Accordingly, the pulse-front tilting approach supports much shorter pulse, reaching 95 fs.

The fact, that the measured spectrum is not as broad as the calculated one, can be explained by imperfect compensation of angular dispersion, as was described in section 2.1. This is also confirmed by the beam profiles, shown and described in section 3.3. The residual angular dispersion , estimated to be around 160 µrad /nm, corresponding to a residual pulse front tilt of about 4.7°, causes the farthest part of the spectrum to be diverging, so it can be limited by the aperture of the used optics. The thin-film polarizer before the autocorrelator can also not work effectively for the part of the spectrum farthest from the central value of 515 nm due to the angle of incidence differing from the Brewster angle. Other effects can also play a significant role in the observed discrepancy between the measured and the calculated spectrum, most notably non-ideal pulse-front tilt angle, causing less than ideal ratio of group velocities of the interacting pulses, and the periodic modulation in the beam profiles causing higher phase mismatch than was presumed.

3.3. Beam profiles

Some descriptive parameters of the beam profiles, together with selected beam profiles, are shown in Fig. 9.

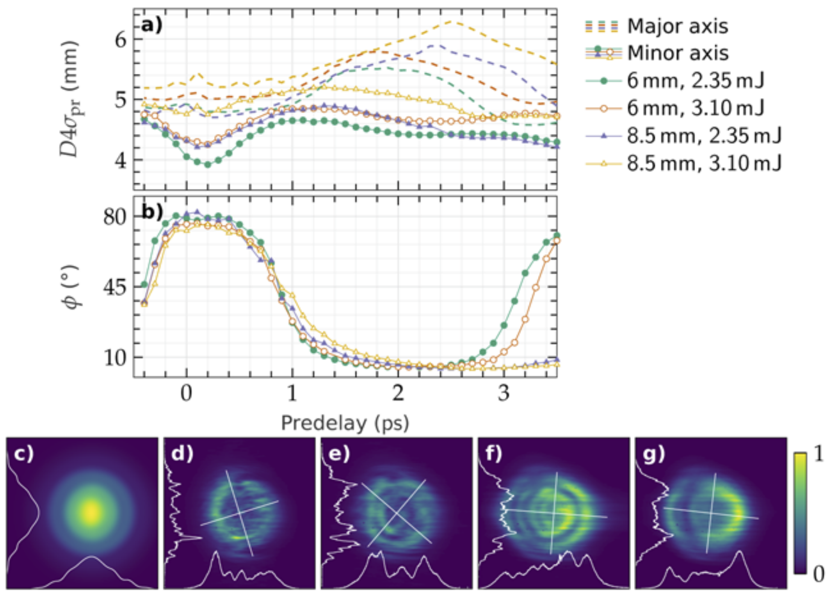

Fig. 9. Descriptive parameters of the beam profiles: Width (a) and azimuth angle (b), beam profile calculated in 8.5 mm long crystal with 3 mJ of energy with predelay of 2.2 ps (c), together with chosen beam profiles measured at a predelay of 0.0 ps (d), 1.0 ps (e), 2.6 ps (f) and 3.5 ps (g). Total area of each beam profile is 7.04 mm × 7.04 mm. The beam profiles were measured in the 8.5 mm thick crystal with an energy of 3.10 mJ.

Ellipticity is around 0.85 at a predelay of 0 ps, where the major axis is close to the Y axis. This is the same orientation and ellipticity as in the beam profile of the driving laser in Fig. 4(b). As the predelay increases to the region of the broadest spectrum (around 2 ps for the thinner crystal and 2.6 ps for the thicker crystal), the beam width in the major axis rises and the azimuth angle decreases – the major axis is rotated to be almost parallel with the X axis. There is no reason for such behaviour to occur in the SHG process and the apparent beam width increase is caused strictly by the spectral broadening and the non-ideal compensation of angular dispersion. As the predelay increases even further, the major axis gets rotated again to the more vertical direction, as the spectrum gets narrower. The widening of the spectrum is particularly well visible in the beam profile shown in Fig. 9(f), measured at the 2.6 ps predelay.

Otherwise, the beam profiles at low predelay are flattish, resembling a ring or a spiral. At zero predelay (Fig. 9(d)), the beam is symmetric and has no central peak. At higher predelays (Fig. 9(e)-(g), peak starts to appear, although it is not in the centre of the beam. This is caused by the spatial walk-off compensation, which was adjusted at one particular predelay close to 0 ps, but should be changed for each predelay individually for the input beams to be centred at the moment, in which they pass each other in the time domain.

The concentric rings develop through the back-conversion, as the intensity and thus the rate of the energy exchange differs radially in the originally Gaussian beam. The development of the rings was predicted by the numerical simulations in Fig. 9(c), where the radial steps are visible in the cross-section. However, they became much more pronounced in the experiment, because the phase mismatch and so also the rate of the back-conversion was larger than was

OPTICS CONTINUUM

assumed. There is a periodic exchange of energy between the interacting pulses. At one radius, corresponding to some intensity level, the energy of the SH pulse can end up in the trough of the energy exchange function, and at another radius it can end up in a crest. With small phase mismatch, as in the numerical simulations, the period of the energy exchange function is larger and the difference between minima and maxima is smaller than with higher phase mismatch, as in the experiments. That is the reason, why we only saw few small steps in the calculated beam profile, but experimentally observed many distinct rings. As the predelay increases beyond the region of the broadest spectrum, the beams do not have enough interaction time for the back-conversion to manifest itself by the ring creation.

Finally, there are horizontal stripes visible in every measured beam profile. Their origin is not directly linked to the SHG process, they appear already in the input beam after the first diffraction grating and become more pronounced at the second one. These intensity modulations can be linked to phase modulations, which negatively influence the SHG and pulse compression processes by introducing phase mismatch and which were originally not calculated with, and so increase the rate of the back-conversion.

3.4. Autocorrelation

Data concerning the pulse duration are shown in Fig. 10.

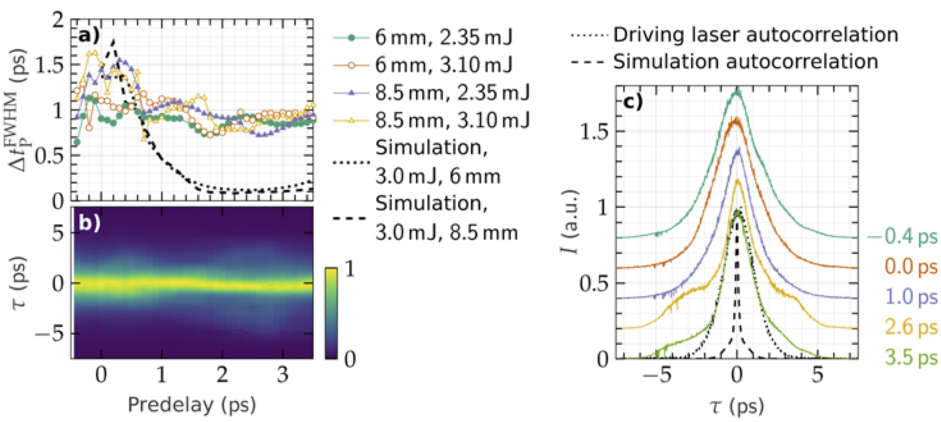

Fig. 10. Measured and simulated pulse duration in dependence on predelay (a). All autocorrelations measured in 8.5 mm long crystal at an energy of 3.10 mJ in dependence on predelay (b). Autocorrelation traces measured at indicated predelays compared with autocorrelation trace of the simulate pulse and autocorrelation trace of the driving laser pulse (c). The numerical simulation is the standard one with crystal thickness of 8.5 mm, predelay of 2.2 ps, and energy 3 mJ, without chirp and with small phase mismatch. The autocorrelation trace of the pulse with added chirp and phase mismatch compensation is undistinguishable on this scale.

The pulse durations in respect to predelay are visible in Fig. 10(a). For the 6 mm long crystal, the minimum pulse duration is around a predelay of 1.8 ps and for the thicker crystal, it is around 2.6 ps. These predelays coincide very well with the predelays with the broadest spectra. The measured pulse duration reaches down to 700 fs, so much longer than the simulated values around 100 fs, also shown in the graph.

How do the autocorrelation traces look like is visible in graph 10b, measured in 8.5 mm long crystal at an energy of 3.10 mJ. Between zero and 1 ps predelay, the autocorrelation trace has typical Gaussian profile. As the predelay is increased, the autocorrelation trace gets narrower, and with predelay larger than 2 ps, pedestal with a narrow peak appears, similar to the one assumed in

Fig. 6. However, the central peak is much longer than it should be, as is evident from the values of pulse duration.

Some particular autocorrelation traces are shown in Fig. 10(c), where the long pedestal and shorter central peak at a predelay of 2.6 ps is nicely visible. The apparent pulse shortening from the duration of the driving laser is rather small. At even larger predelays, the pedestal diminishes. Visually, the autocorrelation traces have width very similar to the duration of the driving laser pulses and the fact, that the SH duration is reduced by approximately one third form the initial 1.66 ps duration is caused mainly by the different fitting function.

The asymmetry of the autocorrelation traces is caused mainly by the non-homogenous beam profile. The beam profile also influences the measured pulse duration itself, as some of the intensity variation in the autocorrelation trace can be caused not by the varying intensity of the temporal profile of the pulse being autocorrelated, but by the varying intensity in the spatial domain. Part of the reason, why the measured pulse duration was longer than the simulated one, could also be the pulse lengthening in the transmissive optical elements in front of the autocorrelator, and part is in the non-ideal pulse-front tilt angle of the input pulses at the fundamental frequency. Additionally, the frequency chirp of the driving laser plays significant role in the pulse compression process and can lead to much longer pulses, if the phase mismatch is not chosen specifically to reduce the frequency chirp's influence. Better results could be obtained with the driving laser pulses compressed to their Fourier transform limit.

Measuring the pulse duration by autocorrelation is also not appropriate given the fact, that it forces one to make initial assumptions about the pulse shape. In the case of this pulse compression technique, each part of the beam experiences different temporal shape [16, Fig. 7] and full spatial and temporal characterization of the pulse by e.g. STRIPED FISH method [20] should be preferred in the future.

4. Current problems and proposed solutions

In this section, we make a list of the observed problems and propose a solution for each of them. We also focus on presenting additional experimental details, which will ease the refinement of this pulse shaping method to actually measure the pulse compression and make it viable for potential applications.

(1) Chirp of the driving laser. The numerical simulations show, that the presence of temporal chirp in the driving laser pulse can have large impact on the pulse shortening process, but the effect would not be visible by observing the conversion efficiency. The effect of chirp can be sidelined by the adjustment of phase-mismatch, but the magnitude of pulse compression will surely be negatively influenced. It would be best to use laser pulses without chirp.

(2) Spatial walk-off pre-compensation. As we have already written, it is important to change the spatial walk-off pre-compensation together with the change in predelay. The spatial walk-off is 71 mrad, which leads to a displacement of 0.6 mm over the length of the longer crystal. It was found in the numerical simulations, that the optimal spatial separation between the input beams at the input face of the crystal is 0.35 mm with a predelay of 2.2 ps. If the predelay is lower, the beam separation should be smaller to achieve highest output peak power. It is important to remember, that in the setup as we presented it, the beam separation is equal to two times the change in the position of the translation stage, before the telescope. After the telescope, the beam displacement is adjusted by the magnification factor. In practice, the correct walk-off pre-compensation can be adjusted individually for every crystal, energy and predelay to achieve the most radially symmetric beam. Value found this way should coincide with the shortest output pulse.

(3) Better diffraction gratings. For our experiments, we used stock diffraction gratings with very limited diffraction efficiency. They also had low damage threshold and we had to increase the beam size on the grating and then reduce it with the telescope. Additionally, these gratings caused periodic intensity modulations, which negatively influenced the SHG process. We recommend using specially designed diffraction gratings and an image relaying telescope without magnification. To calculate the desired grating parameters, one can use e.g. equations (6) and (7) from paper [16].

(4) The design of the telescope. The focal lengths of the lenses should be as long as the space will allow in order to not be limited in available energy by a possible nonlinear effects in the intermediate plane of focus. Also, the depth of field and depth of focus would be greater, which is beneficial in order to image the whole area of the diffraction grating, which is tilted in respect to the optical axis, into the whole length of the nonlinear crystal.

(5) Phase mismatch. Similarly to spatial walk-off pre-compensation, the phase mismatch should be changed by tilting of the nonlinear crystal with every change in predelay or input energy, with the goal of achieving shortest pulse duration. Especially if the driving laser is even slightly chirped, the phase mismatch plays significant role in the pulse shortening process. For example, with the particular chirp we had, change in phase mismatch by $0.15\,\mathrm{mm}^{-1}$ can result in threefold improvement of the pulse compression process. In the BBO crystal, this corresponds to a tilt of around $0.1°$, or one fifth of a revolution of 80 TPI screw with the standard Thorlabs 1 inch mount.

(6) Pulse duration measurement. If autocorrelation is used as a pulse characterization method, then it is crucial to align the beam into the autocorrelator in such way as to obtain symmetrical trace. If the pulse is not propagating in the same direction as is the movement of the delaying stage inside the device, and the beam is not homogenous, this can result in asymmetrical trace, where some observed features can be caused by the intensity changes in beam spatial profile and not the pulse temporal profile. FROG would be better for the full temporal characterization of the pulse profile. We did not made such characterization due to the lack of suitable measurement device. Spatio-temporal characterization can be done by rather time-consuming method of picking parts of the beam with a moving aperture and measuring them separately. In theory, better method would be to use the already mentioned STRIPED FISH technique, but this is not readily available on the market.

Admittedly, these points seem quite simple to follow individually. However, combining them all together is rather intricate matter, requiring long experimental campaign to do methodically and properly.

5. Conclusion

In this paper, we present the first experimental evidence of pulse spectral broadening of Yb:YAG thin disk laser pulses with 1.7 ps in duration by nonlinear second harmonic generation in a type II phase-matched BBO crystal, which hints at ongoing pulse compression. The rate of the spectral broadening is controlled by a time predelay of the faster input pulse. The group velocity mismatch between the three interacting pulses is adjusted to allow for the efficient SHG generation and spectral broadening by tilting of the pulse fronts by a diffraction grating.

The reported experiments follow earlier numerical simulations [16]. Most of the experimental results are in line with the simulated ones, with the same overall trends of efficiency and very similar features in spectrum, autocorrelation and beam profiles visible at correct predelays.

Almost no pulse compression was measured with the use of an autocorrelator. However, in each of the two crystals employed, we have generated pulses with spectral width more than 4 nm. Particularly, we have produced pulses with spectrum 4.5 nm wide, supporting pulses as

OPTICS CONTINUUM

short as 95 fs, in the 8.5 mm long crystal at predelay of 2.6 ps with more than 20 % conversion efficiency. This is more than four times wider than a spectrum generated by SHG from the same laser without any pulse compression technique employed.

Furthermore, we discuss the problems with our measurement and propose a solution for each of them. This should allow one to improve the already well explained and carefully described experimental methods to measure the actual pulse compression in the future, and also improve on the beam quality of the second harmonic compressed beam. Afterwards, the presented method for nonlinear pulse shaping and compression using tilting of the pulse fronts and predelay in SHG could significantly extend the range of the possible applications of the Yb:YAG high-average-power thin-disk lasers into the femtosecond regime.

Funding. European Regional Development Fund (CZ.02.1.01/0.0/0.0/15_006/0000674); Horizon 2020 Framework Programme (739573).

Acknowledgments. We thank the reviewers for their insights.

Disclosures. The authors declare no conflicts of interest.

Data availability. Data underlying the results presented in this paper are not publicly available at this time but may be obtained from the authors upon request.

References

1. Y. Wang and R. Dragila, "Efficient conversion of picosecond laser pulses into second-harmonic frequency using group-velocity dispersion," Phys. Rev. A **41**(10), 5645–5649 (1990).
2. A. Stabinis, G. Valiulis, and E. A. Ibragimov, "Effective sum frequency pulse compression in nonlinear crystals," Opt. Commun. **86**(3-4), 301–306 (1991).
3. Y. Wang and B. Luther-Davies, "Frequency-doubling pulse compressor for picosecond high-power neodymium laser pulses," Opt. Lett. **17**(20), 1459–1461 (1992).
4. A. Umbrasas, J.-C. Diels, J. Jacob, G. Valiulis, and A. Piskarskas, "Generation of femtosecond pulses through second-harmonic compression of the output of a Nd: YAG laser," Opt. Lett. **20**(21), 2228–2230 (1995).
5. T. Zhang, H. Daido, Y. Kato, L. B. Sharma, Y. Izawa, and S. Nakai, "Second-Harmonic Generation of a Picosecond Laser Pulse at High Intensities with Time Predelay," Jpn. J. Appl. Phys. **34**(Part 1, No. 7A), 3546–3551 (1995).
6. R. Danielius, A. Dubietis, A. Piskarskas, G. Valiulis, and A. Varanavicius, "Generation of compressed 600-720-nm tunable femtosecond pulses by transient frequency mixing in a beta-barium borate crystal," Opt. Lett. **21**(3), 216–218 (1996).
7. M. Nisoli, S. De Silvestri, G. Valiulis, and A. Varanavicius, "Fivefold femtosecond pulse compression by sum frequency generation," Appl. Phys. Lett. **68**(25), 3540–3542 (1996).
8. O. Novák, T. Miura, M. Smrž, M. Chyla, S. Nagisetty, J. Mužík, J. Linnemann, H. Turčičová, V. Jambunathan, O. Slezák, M. Sawicka-Chyla, J. Pilar, S. Bonora, M. Divoký, J. Měsíček, A. Pranovich, P. Sikocinski, J. Huynh, P. Severová, P. Navrátil, D. Vojna, L. Horáčková, K. Mann, A. Lucianetti, A. Endo, D. Rostohar, and T. Mocek, "Status of the High Average Power Diode-Pumped Solid State Laser Development at HiLASE," Appl. Sci. **5**(4), 637–665 (2015).
9. M. Smrž, O. Novák, J. Mužík, H. Turčičová, M. Chyla, S. S. Nagisetty, M. Vyvlečka, L. Roškot, T. Miura, J. Černohorská, P. Sikocinski, L. Chen, J. Huynh, P. Severová, A. Pranovich, A. Endo, and T. Mocek, "Advances in High-Power, Ultrashort Pulse DPSSL Technologies at HiLASE," Appl. Sci. **7**(10), 1016 (2017).
10. M. Smrž, J. Mužík, D. Štěpánková, H. Turčičová, O. Novák, M. Chyla, P. Hauschwitz, J. Brajer, J. Kubát, F. Todorov, and T. Mocek, "Picosecond thin-disk laser platform PERLA for multi-beam micromachining," OSA Continuum **4**(3), 940–952 (2021).
11. S. Beyer, C. Grebing, M. Schultze, K. Michel, G. Korn, and T. Metzger, High Average Power Type II Frequency Doubling with a Predelay for Pulse Compression and Peak Intensity Enhancement, in *Conference on Lasers and Electro-Optics*, (OSA Technical Digest, 2018), p. SM3N.4.
12. M. Duda, O. Novák, M. Chyła, H. Turčičová, V. Kubeček, M. Smrž, and T. Mocek, Peak Power Enhancement of Yb:YAG Laser Pulses by Second Harmonic Generation with Time Predelay in Borate Crystals, in *2019 Conference on Lasers and Electro-Optics Europe and European Quantum Electronics Conference*, (Munich, 2019), p. cd_p_11.
13. M. Duda, O. Novák, M. Chyła, V. Kubeček, M. Smrž, and T. Mocek, Shaping of picosecond laser pulses by second harmonic generation with time predelay, in Nonlinear Frequency Generation and Conversion: Materials and Devices XIX, vol. 11264 P. G. Schunemann and K. L. Schepler, eds. (SPIE, 2020), p. 1126413.
14. A. Dubietis, G. Valiulis, G. Tamosauskas, R. Danielius, and A. Piskarskas, "Nonlinear second-harmonic pulse compression with tilted pulses," Opt. Lett. **22**(14), 1071–1073 (1997).
15. A. Dubietis, G. Valiulis, G. Tamosauskas, R. Danielius, and A. Piskarskas, "Nonlinear pulse compression in the ultraviolet," Opt. Commun. **144**(1-3), 55–59 (1997).
16. M. Duda, O. Novák, M. Smrž, A. Lucianetti, V. Kubeček, and T. Mocek, "Numerical study of sum frequency ultrashort pulse compression in borate crystals," J. Opt. Soc. Am. B **37**(11), 3229–3238 (2020).

OPTICS CONTINUUM

17. O. E. Martinez, "Pulse distortions in tilted pulse schemes for ultrashort pulses," Opt. Commun. **59**(3), 229–232 (1986).
18. O. Martinez, "Achromatic phase matching for second harmonic generation of femtosecond pulses," IEEE J. Quantum Electron. **25**(12), 2464–2468 (1989).
19. M. Duda, O. Novák, M. Chyla, M. Smrž, and T. Mocek, "Balancing the conversion efficiency and beam quality of second harmonic generation of a two-picosecond Yb:YAG thin-disk laser," Laser Phys. **30**(2), 025405 (2020).
20. P. Gabolde and R. Trebino, "Single-frame measurement of the complete spatiotemporal intensity and phase of ultrashort laser pulses using wavelength-multiplexed digital holography," J. Opt. Soc. Am. B **25**(6), A25–A32 (2008).